

Baroclinic control of Southern Ocean eddy upwelling near topography

Alice Barthel¹, Andrew M. Hogg², Stephanie Waterman³, and Shane Keating⁴

¹Los Alamos National Laboratory, Los Alamos, NM, USA.

²Research School of Earth Sciences, Australian National University, Canberra, ACT, Australia.

³Department of Earth, Ocean and Atmospheric Sciences, University of British Columbia, Vancouver, BC, Canada.

⁴University of New South Wales, Sydney, NSW, Australia.

Key Points:

- Topography can support localised, enhanced cross-jet isopycnal transport driven by eddies.
 - Transport occurs where baroclinic instability energizes eddies, not where eddy energy is high.
 - In most cases, zonal growth of eddy energy is a more reliable indicator of cross-jet transport than metrics traditionally used.

16 **Abstract**

17 In the Southern Ocean, mesoscale eddies contribute to the upwelling of deep waters along
 18 sloping isopycnals, helping to close the upper branch of the meridional overturning cir-
 19 culation. Eddy energy is not uniformly distributed along the Antarctic Circumpolar Cur-
 20 rent (ACC). Instead, ‘hotspots’ of eddy energy that are associated with enhanced eddy-
 21 induced upwelling exist downstream of topographic features. This study shows that, in
 22 idealized eddy-resolved simulations, a topographic feature in the ACC path can enhance
 23 and localize eddy-induced upwelling. However, the upwelling systematically occurs in
 24 regions where eddies grow through baroclinic instability, rather than in regions where
 25 eddy energy is large. Across a range of parameters, along-stream eddy growth rate is a
 26 more reliable indicator of eddy upwelling than traditional parameterizations such as eddy
 27 kinetic energy, eddy potential energy or isopycnal slope. Ocean eddy parameterizations
 28 should consider metrics specific to the growth of baroclinic instability to accurately model
 29 eddy upwelling near topography.

30 **Plain Language Summary**

31 The Southern Ocean plays an essential role in redistributing heat, salt and biogeochem-
 32 ical tracers of importance in the climate system. In particular, locations in which strong
 33 ocean currents interact with large topographic features are hotspots for eddy-driven up-
 34 ward transport, and are crucial pathways to bring deep, carbon- and nutrient-rich wa-
 35 ters to the surface. The processes which set the location and magnitude of this eddy ‘up-
 36 welling’ remain challenging to understand. This study uses a series of high-resolution ide-
 37 alized simulations in which an ocean jet encounters a piece of topography to investigate
 38 what controls the eddy upwelling near topography. We find that the upwelling due to
 39 eddies occurs in regions where the eddies are growing through a mechanism called ‘baro-
 40 clinic instability’, rather than in regions where eddies are highly energetic or energized
 41 by other mechanisms. Regions of growing eddy energy are a simple, first-order indica-
 42 tor of regions of eddy upwelling, but future parameterisations of transport should con-
 43 sider the mechanism of instability to be more accurate.

44 **1 Introduction**

45 The Southern Ocean is an essential component of the global overturning circula-
 46 tion, which redistributes heat, salt and biogeochemical tracers of importance in the cli-

mate system (J. Marshall & Speer, 2012). In particular, sloping density surfaces (isopycnals) in the Southern Ocean provide an adiabatic route for deep waters to be upwelled to the surface. This along-isopycnal transport brings cold, carbon-rich waters to the surface (Le Quéré et al., 2007), imposing an important control on the Southern Ocean CO₂ sink and contributing to delayed warming of Southern Ocean waters (Armour et al., 2016).

Mesoscale eddies, which are particularly energetic in the Southern Ocean (Fu et al., 2010), play a dominant role in this along-isopycnal transport and therefore can have a critical influence on the associated mass, carbon and heat transports. Eddy activity in the Southern Ocean is not uniform in time or space. Zonal variations along the path of the Antarctic Circumpolar Current (ACC) are punctuated by regions of elevated eddy energy downstream of where the ACC interacts with major topographic features (Sokolov & Rintoul, 2009; Thompson, 2010; Frenger et al., 2015; Foppert et al., 2017), visible both at the surface (e.g. Fu et al., 2010) and at depth (e.g. Thompson & Naveira Garabato, 2014). These hotspots of eddy energy are favourable to stronger cross-jet exchange (Thompson & Sallée, 2012; Dufour et al., 2015) and enhanced upwelling of deep and intermediate waters (Viglione & Thompson, 2016; Tamsitt et al., 2017; Foppert et al., 2017).

Regions of elevated eddy energy are typically co-located with stationary meanders downstream of a topographic obstacle. The presence of these meanders, which are formed by arrested Rossby waves (Hughes & Ash, 2001), introduces non-zonal velocities, which lead to departures from the traditionally-assumed dynamical balances derived from a zonally-integrated view. The stationary meanders play an essential role in balancing zonal momentum and provide a mechanism for rapid barotropic adjustment of the flow to changes in forcing (Thompson & Naveira Garabato, 2014). These meanders appear to dominate the meridional heat transport (Dufour et al., 2012), but such heat transport predominantly occurs through transient eddies acting along the meander structure (Abernathay & Cessi, 2014). The essential role of transient eddies in this heat transport is visible when the transport is calculated in density-depth space (Zika et al., 2013) or following streamlines (Abernathay & Cessi, 2014).

The strength of eddy-induced transport in the Southern Ocean is often assumed to scale linearly with eddy kinetic energy (EKE) along the lines of the classical mixing length hypothesis (Prandtl, 1925; Holloway, 1986). For example, studies investigating the response of Southern Ocean circulation to changes in forcing often examine the re-

sponse of EKE (e.g. Meredith & Hogg, 2006; Hogg et al., 2015; Patara et al., 2016), but few studies diagnose eddy-induced transport. Dufour et al. (2012) noted the increased southward transport due to transient and stationary eddies under increased wind forcing, but did not relate its response to that of EKE. However, there are no direct observations or modelling studies which support a direct, local proportionality between EKE and eddy-induced upwelling. On the contrary, Tamsitt et al. (2017) reports enhanced upwelling upstream of EKE maxima, but does not provide a dynamical explanation for this spatial separation. Likewise, Foppert et al. (2017) noted an offset between eddy heat fluxes and EKE in the Drake Passage, and suggest that the sea surface height deviation (a proxy for eddy potential energy, EPE) is a better indicator of the divergent eddy heat flux and, by extension, eddy upwelling owing to a direct connection to baroclinic instability (Watts et al., 2016). This offset is also found in the idealised simulations of Bischoff & Thompson (2014), which notes that EKE is not co-located with the steepest isopycnal slopes. An examination of how topography modulates eddy-induced upwelling and, further, an identification of the relationship between eddy energy and the mechanisms controlling upwelling location and magnitude are needed, in particular to inform our design of eddy upwelling proxies.

This study focuses on how a single unstable jet in a 2-layer system supports intense, localised, isopycnal upwelling associated with transient eddies. This jet is an analogue for a single filament of the ACC; the simplicity of this system allows unambiguous definition of cross-jet volume transport to quantify eddy upwelling, revealing insights that are not possible in a more comprehensive model. In particular, the question of whether local eddy energy (EE), or one of its constituents (EKE or EPE), is a good indicator of local eddy-induced upwelling is examined. Lastly, we show that a simple parameterisation of eddy-induced upwelling based on the zonal evolution of eddy energy provides a better representation of the zonal variability of upwelling around topography, compared with other proposed parameterisations based on EKE, EPE or time-mean isopycnal slope.

2 Methods

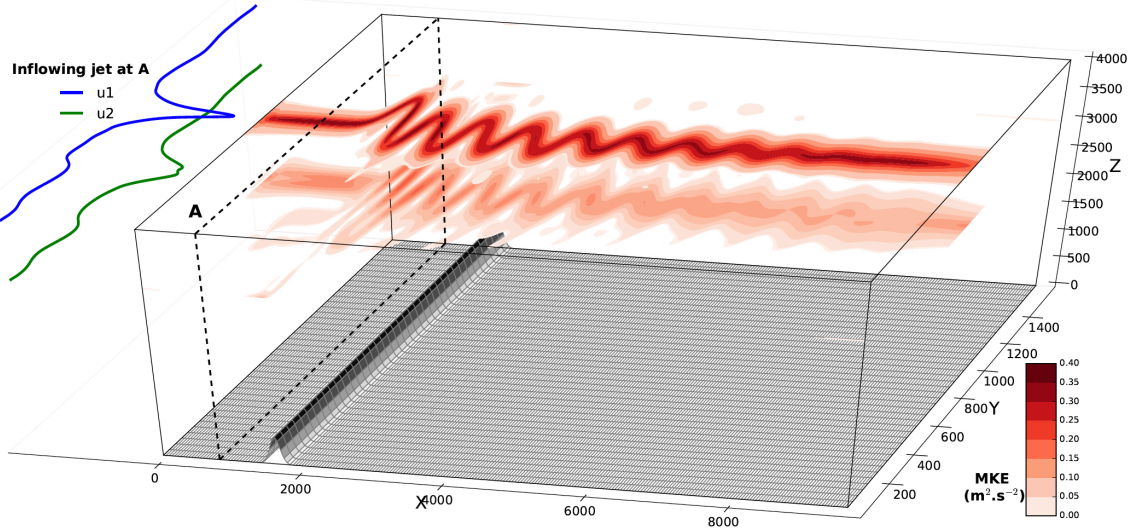
2.1 Model configuration

Our model simulations are designed to represent the interactions between a baroclinic ocean jet and an isolated topographic feature, in a configuration relevant to the

110 Southern Ocean (see Fig. 1). The set-up used is identical to that of Barthel et al. (2017).
111 The model configuration is a channel on a β -plane, with dimensions of 9600 km \times 1600
112 km and a horizontal resolution of 4 km. It consists of two isopycnal layers. We use MOM6
113 (Adcroft et al., 2019) to solve the hydrostatic thickness-weighted primitive equations un-
114 der the Boussinesq approximation. The background horizontal viscosity is parameterised
115 with a biharmonic horizontal viscosity of $A_4 = 1.5 \times 10^9 \text{ m}^4 \text{ s}^{-1}$ to ensure numerical
116 stability, while bottom friction is modelled by a weak quadratic bottom drag (with $C_{drag} =$
117 5×10^{-4}). The dynamics in the interior of the channel are purely adiabatic.

118 The channel is forced to sustain an eastward-flowing jet (Fig. 1) by restoring the
119 stratification at the western boundary. The jet characteristics are representative of a typ-
120 ical frontal jet observed in the Southern Ocean, with a 50-to-150-km-wide jet core con-
121 taining peak velocities of 0.5–1 m s $^{-1}$ (in the upper 1000 m), while velocity below 1000
122 m is of order 0.1 m s $^{-1}$ (Waterman et al., 2013; Sheen et al., 2014). The eastern bound-
123 ary also features a ‘sponge’ region where isopycnal heights are restored to allow the flow
124 to readjust to the inflowing conditions. This boundary forcing of the flow provides a di-
125 rect control of the jet structure at the inflow, as well as prescribing the total zonal trans-
126 port. In this regard, this study differs from wind-driven channel studies which rely on
127 a wind-friction equilibration (e.g. Bischoff & Thompson, 2014; Chapman et al., 2015) and
128 can feature significantly different zonal transports depending on the presence of bottom
129 topography (see Abernathey & Cessi, 2014, their Fig. 8). Stratification is also restored
130 at the northern and southern boundaries, thus sustaining a large-scale meridional isopy-
131 cnal slope, with the upper layer shoaling southward. This combination of forcing allows
132 a non-zero residual overturning circulation to emerge in the domain, as it does in the South-
133 ern Ocean (e.g. G. J. Marshall, 2003; Lumpkin & Speer, 2007).

134 To explore topographic control of eddy-driven isopycnal upwelling, we compare flat-
135 bottom simulations with cases which include either a circular seamount, or a meridional
136 ridge, with a range of heights (0–500m). The range of topographic heights is small (com-
137 pared with the Southern Ocean) because the topography has a disproportionately large
138 effect in a two-layer system.



139 **Figure 1.** Model domain. A prescribed 2-layer jet flows eastward over topography, leading to
 140 stationary meanders downstream of topography. The maximum inflow velocities at section A are
 141 0.7 m.s^{-1} for the upper layer and 0.3 m.s^{-1} for the lower layer.

142 2.2 Quantifying meridional transport

143 We diagnose the eddy-driven upwelling by quantifying the southward volume trans-
 144 port due to transient eddies in the upper, southward-shoaling isopycnal layer. Impor-
 145 tantly, we account for the presence of stationary meanders downstream of topography
 146 by isolating the volume transport across the time-mean jet axis (hereafter the cross-jet
 147 transport). As our simulations have only one southward-shoaling layer, we sidestep the
 148 difficulties of defining a depth-dependent jet axis and focus on the transport by eddies
 149 across the contour of maximum upper-layer time-mean velocity. The transport, T , per-
 150 pendicular to the time-mean velocity field is written as

$$151 T(x, y) = \bar{h}_1 \bar{\mathbf{u}}_1 \times \frac{\bar{\mathbf{u}}_1}{|\bar{\mathbf{u}}_1|} = \bar{h}'_1 \bar{\mathbf{u}}'_1 \times \frac{\bar{\mathbf{u}}'_1}{|\bar{\mathbf{u}}'_1|}, \quad (1)$$

152 where h_1 is the thickness and \mathbf{u}_1 is the horizontal velocity in the upper layer. The over-
 153 bar indicates the time-mean of a quantity, and the prime is the deviation from that mean
 154 (i.e. the eddy component). By construction, only the eddy quantities contribute to the
 155 net transport across the time-mean velocity field. The cross-jet transport, X_{jt} , is defined
 156 on the jet axis:

$$157 X_{jt} = T(x, y_m(x)), \quad (2)$$

158 where y_m is the value of y for which $|\bar{\mathbf{u}}_1|$ is maximal. We count the transport as posi-
 159 tive when it is southward, i.e. when it is associated with upwelling along the isopycnal
 160 layer.

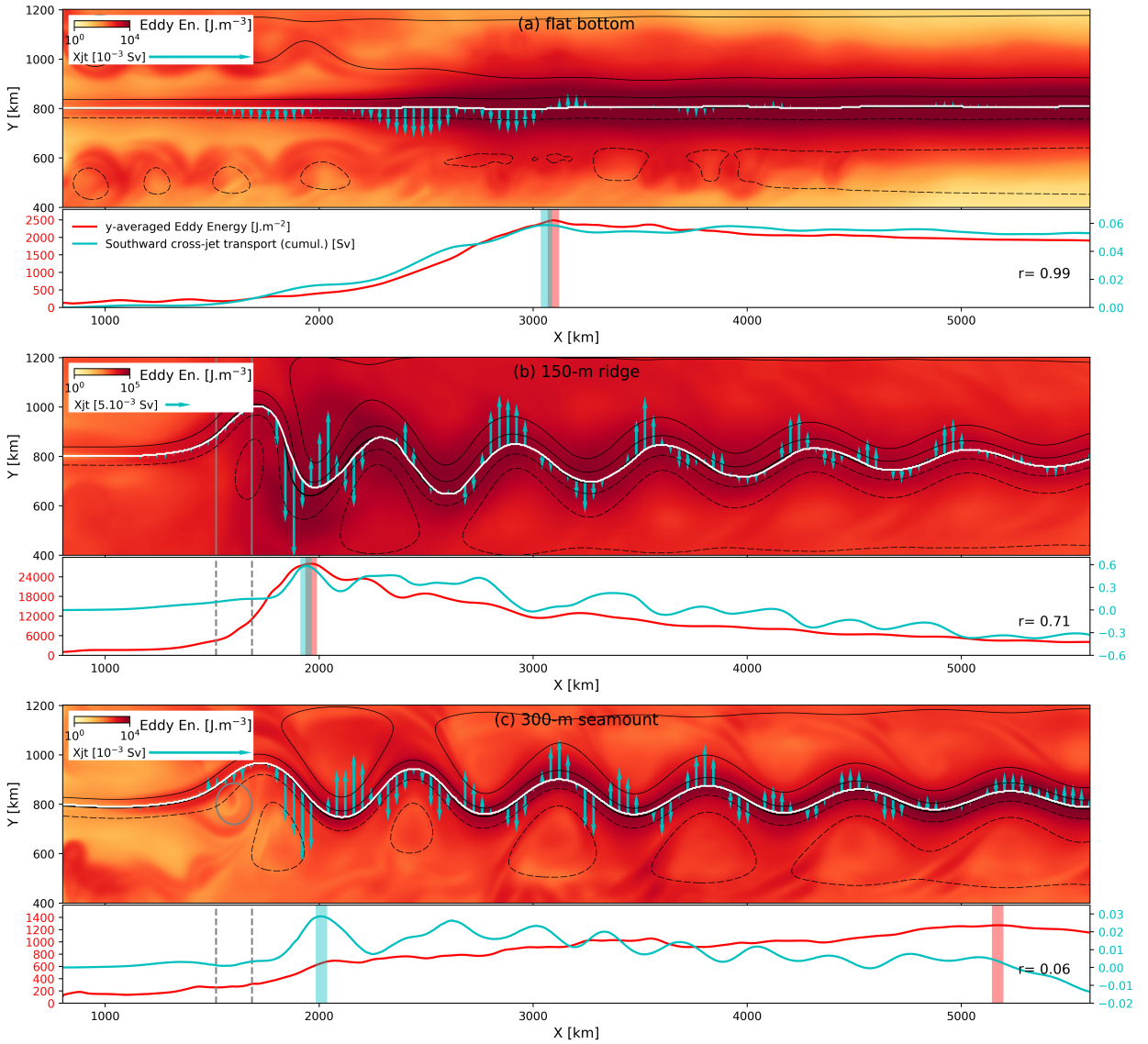
161 The advantage of the above definition is that it allows us to robustly compare the
 162 net transport by eddies in the presence stationary meanders that form downstream of
 163 topographic obstacles. As stationary meanders have significant time-mean meridional
 164 velocities, they would have an alternating signal in southward and northward transport
 165 across a fixed latitude line (see Hallberg & Gnanadesikan, 2001, for a discussion on trans-
 166 port across streamlines versus fixed contours). Calculating the cross-jet transport at the
 167 jet axis allows a more meaningful comparison of net cross-jet transport between cases
 168 with and without jet meanders.

169 3 Results

170 3.1 Eddy-driven upwelling

171 The mean flow state from three selected runs is presented in Fig. 2. In each case
 172 the inflowing jet becomes unstable as it evolves eastward. The eddy energy (sum of EKE
 173 and EPE; indicated by colours in the upper panel of each subplot) has a distinct spa-
 174 tial pattern, growing with x as the flow evolves, with an along-stream maximum (high-
 175 lighted by the red vertical bar in the lower panel). Eddy energy then remains constant
 176 or decays with further distance downstream. The qualitative evolution of eddy energy
 177 is similar in all three cases, although the zonal extent of the eddy energy growth region
 178 and the magnitude of the eddy energy depends on the nature of the topography. Sim-
 179 ilar results are obtained if we examine EKE and EPE individually (not shown).

188 The transient motions lead to an eddy-induced upwelling, quantified by the eddy-
 189 induced thickness transport across the time-mean jet axis (cyan arrows in Fig. 2). This
 190 transport also has zonal variations along the jet axis. In the case of the jet evolving over
 191 a flat bottom (Fig. 2a), the transport is southward, and preferentially takes place in a
 192 limited region ($1500 \text{ km} < x < 3100 \text{ km}$). Further downstream, both southward and
 193 northward flux can occur locally, but these fluxes contribute little to the net transport.
 194 The bulk of the eddy-induced southward transport is localised in the region of eddy en-
 195 ergy growth, with a 99% correlation between the zonal variations in the zonally integrated
 196 cumulative transport and local eddy energy (Fig. 2a, lower subpanel).



180 **Figure 2.** Eddy energy and cross-jet transport for a) flat bottom, b) 150m-tall ridge, c) 300m-tall seamount. In each subplot, the upper panel shows eddy energy (colours), the time-mean
 181 upper layer streamfunction (black contours), the time-mean jet axis (white line) and southward
 182 cross-jet volume transport (cyan arrows); the lower panel shows eddy energy integrated across
 183 the jet (red line, with the maximum value indicated by the vertical red bar) and the zonally in-
 184 tegrated cumulative southward cross-jet transport (cyan line, with the maximum value indicated
 185 by the vertical cyan bar). Note that the 150 m ridge case (panel b) has significantly higher eddy
 186 energy and cross-jet transport, and thus has a different colour scale and arrow length scale.
 187

In the presence of topography (illustrated by the 150 m ridge case; Fig. 2b), localised regions of enhanced eddy-induced cross-jet transport persist. The signature of the stationary meanders is visible in the eddy-induced cross-jet transport variability (manifested as alternating regions of southward and northward transport), making it difficult to distinguish the net effect of eddies. It is therefore especially helpful in this case to consider zonally integrated cumulative transport (cyan line, Fig. 2b, lower subpanel). This metric shows that the region immediately downstream of the ridge ($x = 1500 - 2000$ km) contributes significantly to the net southward transport relative to the regions further downstream. Around $x \approx 2000$ km (highlighted by the cyan vertical bar), there is a transition between a region of net southward transport ($x < 2000$ km) and a region of net northward transport ($x > 2000$ km). In some cases, the cumulative transport at $x = 6000$ km is northward, which may be due to the lack of disturbances to break down the meanders downstream. The close relationship between zonal growth of eddy energy and southward cross-jet transport, seen in the flat bottom case, also holds in the 150m ridge case (71% correlation).

Most of the simulations with topography conducted in this study provided results that are qualitatively similar to the 150m ridge case (not shown). However, the third case presented in Fig. 2, that with a 300 m high seamount, is one of the exceptions. This case is consistent with the results above in that it shows a qualitatively similar zonal evolution of eddy energy, and regions of preferential cross-jet transport immediately downstream of topography, but differs in the lack of correlation between along-stream eddy growth and cumulative southward transport. The break-down in this relationship provides insights into the underlying dynamics at play, and is explored in more detail in the next section.

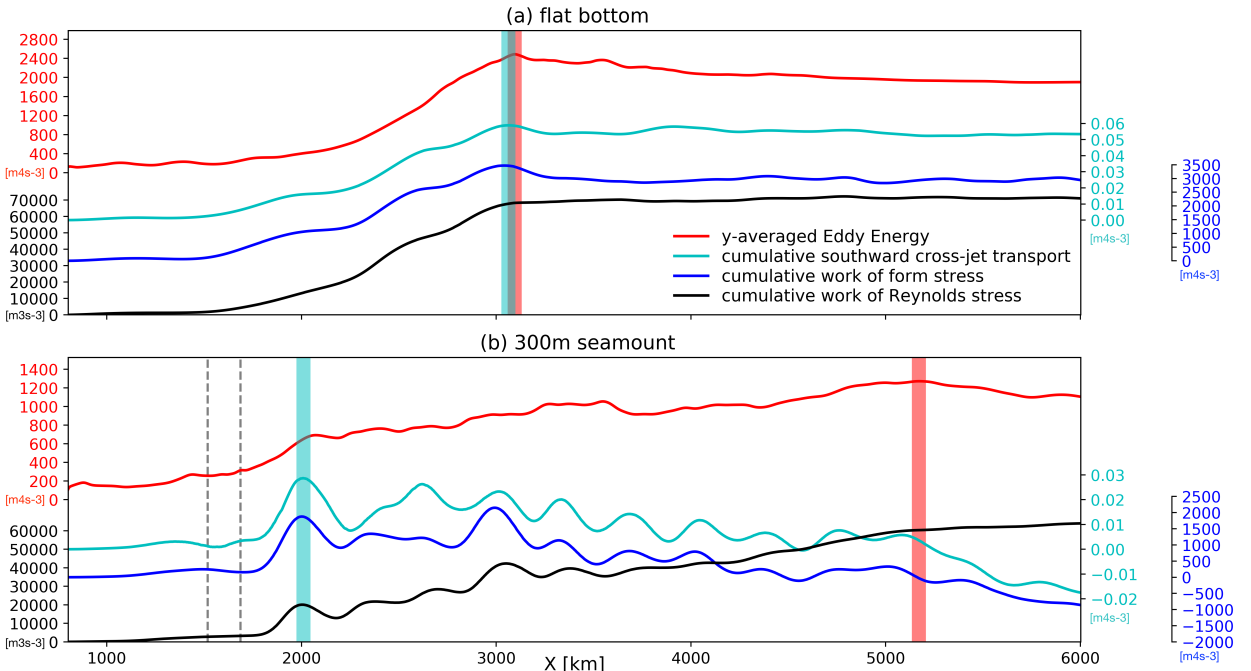
In summary, two main points emerge from examination of the along-stream variations of eddy energy and transport in these idealised simulations. First, the presence of topography leads to enhanced eddy-induced cross-jet transport localised immediately downstream of the topographic obstacle, relative to the same jet evolving over a flat bottom. The magnitude and location of the eddy-induced transport depend on the properties of the topography present. Second, eddy energy and eddy-induced cross-jet transport ('eddy upwelling') have distinct zonal distributions. This transport tends to be localised in the region of along-stream eddy growth, but exceptions can occur where eddy-induced transport occurs in a region of smaller zonal extent than eddy energy growth.

230 **3.2 Mechanism for topographic control**

231 We probe the dynamics underpinning the differing spatial distributions of eddy en-
 232 ergy and eddy-induced transport by looking at the two instability mechanisms that en-
 233 ergise the eddy field in the 300 m seamount case (Fig. 3b), and comparing them with
 234 the flat-bottom case (Fig. 3a). Following the thickness-weighted energetics approach used
 235 in Aiki & Richards (2008) and Barthel et al. (2017), we diagnose the eddy-mean flow en-
 236 ergy conversions due to 1) the work of interfacial form stress, $-\widehat{\mathbf{u}_1} \cdot \overline{h'_1 \nabla \phi'_1}$ (where ϕ_1
 237 is the Montgomery potential and ' denotes the anomaly from the , time mean), respon-
 238 sible for the generation of eddy energy in baroclinic instability (dark blue lines), and 2)
 239 the work of Reynolds stress associated with horizontal convergence of momentum in the
 240 upper layer, associated with barotropic instability (black lines) $\rho_0 \widehat{\mathbf{u}_1} \cdot \nabla \cdot \overline{(h_1 \mathbf{u}_1'' \otimes \mathbf{u}_1'')}$,
 241 where $\widehat{\mathbf{u}_1}$ and \mathbf{u}_1'' are the thickness-weighted mean upper-layer velocity and the devia-
 242 tion from that mean, respectively. The outer product of two vectors is denoted by \otimes ,
 243 and ρ_0 is the reference density of the Boussinesq approximation (see Barthel et al., 2017,
 244 for the full derivation).

256 The 300 m seamount is a helpful case to disentangle the contributions of form stress
 257 and Reynolds stress because they have distinct zonal patterns (Fig. 3b). These patterns
 258 indicate that the eddy-induced transport is associated exclusively with baroclinic insta-
 259 bility (i.e. positive conversion of energy into the eddy field via form stress). This rela-
 260 tionship is consistent with our conceptual understanding that baroclinic instability con-
 261 tributes to flattening isopycnals, and with observations in Drake Passage that indicate
 262 the eddy heat flux is best aligned with the production of EPE (Watts et al., 2016; Fop-
 263 pert et al., 2017). These results further suggest that the zonally-averaged link between
 264 interfacial form stress and meridional thickness flux (e.g. Olbers et al., 2004) may ap-
 265 ply at the local scale. Understanding that the mechanism for eddy-induced transport is
 266 baroclinic instability acting as a source of eddy energy is consistent with the alignment
 267 of the region of eddy upwelling with the region of along-stream eddy growth, rather than
 268 with regions of elevated eddy energy.

269 The relationship between eddy upwelling and the action of eddy form stress in en-
 270 ergising the eddy field is robust across all simulations, both with and without topogra-
 271 phy. In most cases, the region of southward eddy transport extends over the entire re-
 272 gion of along-stream eddy growth because both energy conversion terms have the same



245 **Figure 3.** Zonal distributions of energy conversion terms when an unstable jet evolves over
 246 (a) a flat bottom, (b) encounters a 300m-tall seamount. The total eddy energy averaged over the
 247 channel (red), the along-jet cumulative eddy-driven southward transport across the time-mean
 248 jet ('eddy upwelling') (light blue), the along-jet cumulative work of interfacial form stress due
 249 to baroclinic instability (dark blue) and cumulative work by Reynolds stress due to barotropic
 250 instability (black) are shown. The latter energy conversions terms are both calculated for the
 251 upper layer, and are positive when energy is fluxed from the mean into the eddy field. The grey
 252 dashed lines indicate the half-width of the topography. For each simulation, the location of max-
 253 imum total eddy energy is marked by the red shading (indicating the transition between regions
 254 of along-stream eddy growth and decay), while the cyan shading marks a significant transition
 255 between southward and northward cross-jet eddy transport.

273 zonal patterns, as illustrated by the flat bottom case (Fig. 3a). Nevertheless, it is im-
 274 portant to keep in mind that baroclinic instability alone provides the dynamical mech-
 275 anism to generate cross-jet transport and eddy upwelling. As such, it is possible that along-
 276 stream eddy growth can occur in regions without net southward eddy transport (i.e. with-
 277 out active baroclinic instability) when, for instance, horizontal shear instability is respon-
 278 sible for eddy energy growth. This scenario is nicely illustrated by the 300 m seamount
 279 case (Fig. 3b).

These examples speak to the method by which topography influences the eddy-induced transport. We infer that the topographic obstacles affect the flow in such a way that either baroclinic or barotropic instability, or both, are enhanced. In some, but not all, cases there is a strong correspondence between these two different instability mechanisms. However, southward eddy-induced transport is only dependent on the action of baroclinic instability, where isopycnal interfaces slump to release available potential energy into the eddy field.

4 Implications for eddy parameterisations

Our results suggest that energy conversion terms are an unambiguous indicator of eddy-induced cross-jet transport, however, we recognize that these are unlikely to be practical indicators of eddy upwelling in coarse resolution models. Our analysis also indicates that the along-stream growth/decay of eddy energy may be a valuable predictor of eddy upwelling in many cases, and hence may inspire new eddy parameterisations for coarsely-resolved models. Thus, in this section, we assess whether a coarsely-resolved zonal pattern of eddy energy may be used to estimate the cross-jet transport occurring in that region. For that purpose, we compare transport estimates obtained from assuming transport is proportional to the rate of along-stream eddy energy growth to those employing other common parameterizations for eddy upwelling based on large-scale variables, such as the mean isopycnal slope, EKE and EPE. Specifically we consider parameterizations based on the following relationships:

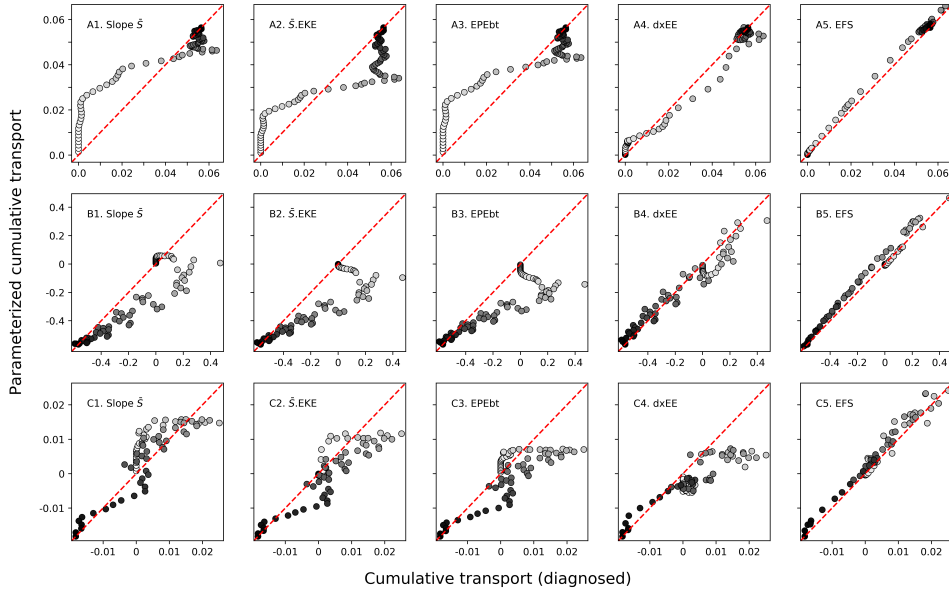
- (a) Transport can be parameterised as a constant diffusivity applied to the time-mean isopycnal slope (\bar{S}): $X_{jt}^{GM}(x) = \kappa\bar{S} + B$, with a constant $\kappa = A$, inspired by Gent & McWilliams (1990);
- (b) The diffusivity κ is proportional to EKE: $X_{jt}^J(x) = A.EKE \cdot \bar{S} + B$, inspired by Jansen et al. (2015);
- (c) Eddy transport is proportional to the barotropic EPE: $X_{jt}^{EPE}(x) = A.EPEbt + B$, with $EPEbt = \frac{\rho_0}{2}g\bar{\eta'^2}$ (ρ_0 : reference density; g : gravitational acceleration; η' : sea surface height), inspired by Foppert et al. (2017);
- (d) Eddy transport is proportional to the rate of along-stream eddy energy growth: $X_{jt}^{dxEE}(x) = A.\frac{d}{dx}EE + B$ where EE denotes total eddy energy.

- 310 (e) Eddy transport is proportional to the local eddy form stress (EFS): $X_{jt}^{EFS}(x) =$
 311 $A.EFS + B$, used as a reference in this exercise.

312 To compare the relative performance of these parameterisations in our model configu-
 313 ration, the large-scale variable on which each parameterisation is based (\bar{S} , EKE, EPEbt,
 314 EE or EFS) was smoothed and sub-sampled to a 80km horizontal resolution, roughly equiv-
 315 alent to output from a 1° ocean model. In each case, a least-squares fit was performed
 316 to determine the parameters A and B that minimise the total error in transport over the
 317 domain. The parameterised transport is then compared to the modeled transport in four
 318 different cases (Fig. 4). We place a caveat on the results that follow, which is that the
 319 list of eddy parameterisations evaluated is by no means exhaustive. In addition, the com-
 320 parison presented here allow the parameters to be fitted for each case, while a more sys-
 321 tematic parameterisation may require the parameter values to work uniformly across cases.

322 Results from this exercise confirm the conclusions from the previous section. Lo-
 323 cal values of energy reservoirs, such as EPE, are not a good indicator of cross-jet trans-
 324 port (e.g. Fig. 4.A3 for the flat-bottom case). The zonal variations in EPE and trans-
 325 port are so different that minimising the total error leads to applying a small southward
 326 transport almost uniformly over the whole domain, leading to compensating over-estimated
 327 transport upstream (light gray) and under-estimated transport further downstream (dark
 328 gray). Similarly, the other relationships based on time-mean isopycnal slope and EKE
 329 (Fig. 4A.1-2) fail to capture the zonal pattern of transport, with the best parameteri-
 330 sation being an almost uniform transport of small magnitude.

331 In contrast, the zonal growth rate of total eddy energy, $\frac{d}{dx}EE$, is able to reproduce
 332 the zonal variations in eddy transport, producing a parameterised transport which ad-
 333 equately portrays regions of little to no transport, and regions of localised, enhanced trans-
 334 port. Local eddy form stress is overall the best indicator for eddy transport, but is un-
 335 likely to be readily available output from climate models or observations. In the absence
 336 of eddy form stress, the zonal growth of eddy energy may be a valuable indicator of where
 337 eddy-induced transport occurs, and outperforms commonly used parameterisations of
 338 eddy upwelling, in most cases considered in this study (see Supporting Information). One
 339 exception is the 300m seamount case (Fig. 4.C1-4) where the relationship between cross-
 340 jet transport and the along-stream rate of change of total eddy energy breaks down (Fig.
 341 3b) due to the influence of barotropic instability in generating eddy energy.



342 **Figure 4.** Parameterised cumulative southward transport across the jet axis plotted against
 343 the resolved cumulative transport, at each zonal gridpoint along the time-mean jet axis, for A.
 344 flat bottom, B. 150m ridge, and C. 300m seamount. Data points are colored from light to dark
 345 as we move downstream. In each case, the parameterisation is the best linear fit (by least-square
 346 method) that minimises the total error between local values of transport and local 1) time-mean
 347 cross-jet isopycnal slope \bar{S} , 2) EKE times \bar{S} , 3) barotropic EPE ($EPEbt$), 4) zonal growth of
 348 total eddy energy ($dxEE$), and 5) eddy form stress (EFS), where each variable was smoothed and
 349 sub-sampled to a 80km resolution.

350 5 Discussion

351 This study highlights that eddy-driven cross-jet transport within a shoaling isopyc-
 352 nal occurs in regions of eddy energy growth through baroclinic instability. The pres-
 353 ence of topography leads to enhanced eddy upwelling in the region immediately down-
 354 stream of the obstacle (especially in the first meander) because it modifies the growth
 355 of baroclinic instability. The idealised set-up allows exact calculations of quantities not
 356 usually diagnosed in global climate models, and the simulations performed in this study
 357 provide a plausible mechanism explaining the location of the upwelling pathways from
 358 Tamsitt et al. (2017) which occurs in regions upstream of EKE maxima, and further the
 359 offset between the divergent eddy heat flux and EKE discussed by Foppert et al. (2017).
 360 Simple parameterisations based on mean isopycnal slope, EKE and EPE fail to repro-

361 duce this strong, localised, eddy transport near topography. In most cases, the along-
 362 stream growth of eddy energy is a good indicator for southward transport, with the ex-
 363 ception of cases where barotropic instability and baroclinic instability have distinct growth
 364 regions (e.g. a steep isolated seamount; Fig. 4C4).

365 The benefit of an idealized set-up is that it allows exact calculations of both the
 366 eddy form stress and the Reynolds stress, and we can thereby attribute dynamical rel-
 367 evance between the two without ambiguity (noting that these quantities are not usually
 368 diagnosed from global climate models or observations). However, the simplified verti-
 369 cal structure in this two-layer system leads to an exaggerated impact of topography, as
 370 small values of topography are more dynamically relevant to the ACC. Idealised simu-
 371 lations may also over-stimulate barotropic instability near topography (e.g., Barthel et
 372 al., 2017; Youngs et al., 2017). Despite this caveat, we argue that the two-layer set up
 373 provides useful dynamical insight, given that evidence of mixed barotropic-baroclinic in-
 374 stability is also observed in the Drake Passage (Foppert, 2019) and may be important
 375 for the momentum balance in the ACC (Constantinou & Hogg, 2019).

376 In this study, we focused only on eddy-induced isopycnal thickness fluxes and showed
 377 that eddy-driven upwelling does not occur in regions of high eddy energy, but rather in
 378 regions of along-stream eddy energy growth by baroclinic instability. However, the pres-
 379 ence of high eddy energy, and potentially high EKE in particular, may contribute to en-
 380 hancing other types of transport, such as the upwelling of tracers through increased isopy-
 381 cnal stirring (Abernathy & Ferreira, 2015; Dufour et al., 2015). In addition, the net merid-
 382 ional transport in the Southern Ocean is forced by a combination of factors, including
 383 wind stress, surface buoyancy fluxes and diabatic processes in the surface mixed layer;
 384 these factors are dominant where layers outcrop at the surface and emphasise the role
 385 of the vertical structure of eddy processes in the ACC that are omitted from this study.
 386 Results from the adiabatic simulations considered in this study best inform on interior
 387 upwelling processes, away from frictional boundaries such as the surface and bottom Ek-
 388 man layers, and away from locations where diabatic mixing dominates (e.g. close to rough
 389 topography).

390 Keeping in mind the above caveats, the detailed dynamical analysis of these ide-
 391 alised simulations provides an important insight: assuming that high values of EKE and/or
 392 EPE indicate regions of strong eddy-driven transport is a misconception. In the South-

393 ern Ocean there is increasing evidence of mixed instability near topography, where both
 394 barotropic and baroclinic instability mechanisms contribute to the dynamics (Youngs
 395 et al., 2017; Barthel et al., 2017; Foppert, 2019). The distinct role of each instability mech-
 396 anism, and their interaction, need to be considered when developing eddy transport pa-
 397 rameterisations that will respond physically to changes in ocean dynamics.

398 6 Open Research

399 The simulation data and scripts used in the study are freely available on the Zen-
 400 odo repository at DOI: 10.5281/zenodo.2542957.

401 Acknowledgments

402 AB was partially supported by the RGCM program of the US Department of Energy.
 403 SW acknowledges support from the Australian Research Council (DE120102927) and the
 404 National Science and Engineering Research Council of Canada (22R23085). SRK was
 405 supported by a UNSW Silverstar research grant. This research was undertaken on the
 406 NCI National Facility in Canberra, Australia, supported by the Australian Commonwealth
 407 Government.

408 References

- 409 Abernathey, R., & Cessi, P. (2014). Topographic Enhancement of Eddy Efficiency
 410 in Baroclinic Equilibration. *Journal of Physical Oceanography*, 44(8), 2107–2126.
 411 doi: 10.1175/JPO-D-14-0014.1
- 412 Abernathey, R., & Ferreira, D. (2015). Southern Ocean isopycnal mixing and ven-
 413 tilation changes driven by winds. *Geophysical Research Letters*, 42, 10357–10365.
 414 doi: 10.1002/2015GL066238
- 415 Adcroft, A., Anderson, W., Balaji, V., Blanton, C., Bushuk, M., Dufour, C. O., ...
 416 Zhang, R. (2019). The GFDL Global Ocean and Sea Ice Model OM4.0: Model
 417 Description and Simulation Features. *J. Adv. Model. Earth Syst.*, 3167–3211. doi:
 418 10.1029/2019MS001726
- 419 Aiki, H., & Richards, K. J. (2008). Energetics of the Global Ocean: The Role of
 420 Layer-Thickness Form Drag. *Journal of Physical Oceanography*, 38(9), 1845–1869.
 421 doi: 10.1175/2008JPO3820.1
- 422 Armour, K. C., Marshall, J., Scott, J. R., Donohoe, A., & Newsom, E. R. (2016).

- 423 Southern Ocean warming delayed by circumpolar upwelling and equatorward
424 transport. *Nature Geoscience*, 9(7), 549–554. doi: 10.1038/ngeo2731
- 425 Barthel, A., McC. Hogg, A., Waterman, S., & Keating, S. (2017). Jet–Topography
426 Interactions Affect Energy Pathways to the Deep Southern Ocean. *Journal of*
427 *Physical Oceanography*, 47(7), 1799–1816. doi: 10.1175/JPO-D-16-0220.1
- 428 Bischoff, T., & Thompson, A. F. (2014). Configuration of a Southern Ocean Storm
429 Track. *Journal of Physical Oceanography*, 44, 3072–3078. doi: 10.1175/JPO-D-14
430 -0062.1
- 431 Chapman, C. C., Hogg, A. M., Kiss, A. E., & Rintoul, S. R. (2015). The Dynamics
432 of Southern Ocean Storm Tracks. *Journal of Physical Oceanography*, 45, 884–903.
433 doi: 10.1175/JPO-D-14-0075.1
- 434 Constantinou, N. C., & Hogg, A. M. (2019). Eddy saturation of the southern ocean:
435 A baroclinic versus barotropic perspective. *Geophysical Research Letters*, 46(21),
436 12202–12212. Retrieved from <https://agupubs.onlinelibrary.wiley.com/doi/abs/10.1029/2019GL084117> doi: 10.1029/2019GL084117
- 437 Dufour, C. O., Griffies, S. M., de Souza, G. F., Frenger, I., Morrison, A. K.,
438 Palter, J. B., . . . Slater, R. D. (2015). Role of Mesoscale Eddies in Cross-
439 Frontal Transport of Heat and Biogeochemical Tracers in the Southern
440 Ocean. *Journal of Physical Oceanography*, 45(12), 3057–3081. Retrieved
441 from <http://journals.ametsoc.org/doi/10.1175/JPO-D-14-0240.1> doi:
442 10.1175/JPO-D-14-0240.1
- 443 Dufour, C. O., Sommer, L. L., Zika, J. D., Gehlen, M., Orr, J. C., Mathiot, P., &
444 Barnier, B. (2012). Standing and transient eddies in the response of the Southern
445 Ocean meridional overturning to the Southern annular mode. *Journal of Climate*,
446 25, 6958–6974. doi: 10.1175/JCLI-D-11-00309.1
- 447 Foppert, A. (2019). Observed storm track dynamics in drake passage. *Journal of*
448 *Physical Oceanography*, 49(3), 867–884. doi: 10.1175/JPO-D-18-0150.1
- 449 Foppert, A., Donohue, K. A., Watts, D. R., & Tracey, K. L. (2017). Eddy heat flux
450 across the antarctic circumpolar current estimated from sea surface height stan-
451 dard deviation. *Journal of Geophysical Research: Oceans*, 122(8), 6947–6964. doi:
452 10.1002/2017JC012837
- 453 Frenger, I., Münnich, M., Gruber, N., & Knutti, R. (2015). Southern Ocean eddy
454 phenomenology. *Journal of Geophysical Research: Oceans*, 120, 7413–7449. doi:

- 456 10.1002/2015JC011047
- 457 Fu, L.-L., Chelton, D., Le Traon, P.-Y., & Morrow, R. (2010). Eddy Dynamics From
458 Satellite Altimetry. *Oceanography*, 23(4), 14–25. doi: 10.5670/oceanog.2010.02
- 459 Gent, P. R., & McWilliams, J. C. (1990). *Isopycnal Mixing in Ocean Circulation
460 Models* (Vol. 20) (No. 1). doi: 10.1175/1520-0485(1990)020<0150:IMIOCM>2.0.CO;
461 2
- 462 Hallberg, R., & Gnanadesikan, A. (2001). An Exploration of the Role of Transient
463 Eddies in Determining the Transport of a Zonally Reentrant Current. *Journal of
464 Physical Oceanography*, 31, 3312–3330.
- 465 Hogg, A. M., Meredith, M. P., Chambers, D. P., Abrahamsen, E. P., Hughes,
466 C. W., & Morrison, A. K. (2015). Recent trends in the Southern Ocean
467 eddy field. *Journal of Geophysical Research C: Oceans*, 120, 257–267. doi:
468 10.1002/2014JC010470
- 469 Holloway, G. (1986). Estimation of oceanic eddy transports from satellite altimetry.
470 *Nature*, 323, 243-244.
- 471 Hughes, C. W., & Ash, E. R. (2001). Eddy forcing of the mean flow in the
472 Southern Ocean. *Journal of Geophysical Research*, 106(C2), 2713. doi:
473 10.1029/2000JC900332
- 474 Jansen, M. F., Adcroft, A. J., Hallberg, R., & Held, I. M. (2015). Parameterization
475 of eddy fluxes based on a mesoscale energy budget. *Ocean Modelling*, 92, 28–41.
476 doi: 10.1016/j.ocemod.2015.05.007
- 477 Le Quéré, C., Rödenbeck, C., Buitenhuis, E. T., Conway, T. J., Langenfelds,
478 R., Gomez, A., ... Heimann, M. (2007). Saturation of the southern ocean
479 CO₂ sink due to recent climate change. *Science*, 316(5832), 1735–1738. doi:
480 10.1126/science.1136188
- 481 Lumpkin, R., & Speer, K. (2007). Global Ocean Meridional Overturning. *Journal of
482 Physical Oceanography*, 37(10), 2550–2562. doi: 10.1175/JPO3130.1
- 483 Marshall, G. J. (2003). Trends in the Southern Annular Mode from Ob-
484 servations and Reanalyses. *Journal of Climate*, 16(24), 4134–4143. doi:
485 10.1175/1520-0442(2003)016<4134:TSAM>2.0.CO;2
- 486 Marshall, J., & Speer, K. (2012, feb). Closure of the meridional overturning cir-
487 culation through Southern Ocean upwelling. *Nature Geoscience*, 5(3), 171–180.
- 488 Retrieved from <http://www.nature.com/doifinder/10.1038/ngeo1391> doi:

- 489 10.1038/ngeo1391
- 490 Meredith, M. P., & Hogg, A. M. (2006). Circumpolar response of Southern Ocean
491 eddy activity to a change in the Southern Annular Mode. *Geophysical Research
492 Letters*, 33(16), 2–5. doi: 10.1029/2006GL026499
- 493 Olbers, D., Borowski, D., Völker, C., & Wolff, J. O. (2004). The dynamical bal-
494 ance, transport and circulation of the antarctic circumpolar current. *Antarc-
495 tic science*, 16(4), 439–470. Retrieved from [http://dx.doi.org/10.1017/
496 S0954102004002251](http://dx.doi.org/10.1017/S0954102004002251) doi: 10.1017/S0954102004002251
- 497 Patara, L., Böning, C. W., & Biastoch, A. (2016). Variability and trends in South-
498 ern Ocean eddy activity in 1/12° ocean model simulations. *Geophysical Research
499 Letters*, 43(9), 4517–4523. doi: 10.1002/2016GL069026
- 500 Prandtl, L. (1925). Bericht ber untersuchungen zur ausgebildeten turbulenz. *Z.
501 Angew. Math. Mech.*, 5, 136.
- 502 Sheen, K. L., Naveira Garabato, A. C., Brearley, J. A., Meredith, M. P., Polzin,
503 K. L., Smeed, D. A., ... Watson, A. J. (2014). Eddy-induced variability in
504 Southern Ocean abyssal mixing on climatic timescales. *Nature Geoscience*, 7(8),
505 577–582. doi: 10.1038/ngeo2200
- 506 Sokolov, S., & Rintoul, S. R. (2009). Circumpolar structure and distribution of
507 the Antarctic Circumpolar Current fronts: 1. Mean circumpolar paths. *Journal of
508 Geophysical Research: Oceans*, 114, C11018. doi: 10.1029/2008JC005108
- 509 Tamsitt, V., Drake, H. F., Morrison, A. K., Talley, L. D., Dufour, C. O., Gray,
510 A. R., ... Weijer, W. (2017). Spiraling pathways of global deep waters to
511 the surface of the Southern Ocean. *Nature Communications*, 8(1), 1–10. doi:
512 10.1038/s41467-017-00197-0
- 513 Thompson, A. F. (2010). Jet Formation and Evolution in Baroclinic Turbulence
514 with Simple Topography. *Journal of Physical Oceanography*, 40(2), 257–278. doi:
515 10.1175/2009JPO4218.1
- 516 Thompson, A. F., & Naveira Garabato, A. C. (2014). Equilibration of the Antarctic
517 Circumpolar Current by Standing Meanders. *Journal of Physical Oceanography*,
518 44(7), 1811–1828. doi: 10.1175/JPO-D-13-0163.1
- 519 Thompson, A. F., & Sallée, J. (2012). Jets and Topography: Jet Transitions and
520 the Impact on Transport in the Antarctic Circumpolar Current. *Journal of Physi-
521 cal Oceanography*, 42(6), 956–972. doi: 10.1175/JPO-D-11-0135.1

- 522 Viglione, G. a., & Thompson, A. F. (2016). Lagrangian pathways of upwelling in the
523 Southern Ocean. *Journal of Geophysical Research: Oceans*, 121(8), 6295–6309.
524 doi: 10.1002/2016JC011773
- 525 Waterman, S., Naveira Garabato, A. C., & Polzin, K. L. (2013). Internal Waves and
526 Turbulence in the Antarctic Circumpolar Current. *Journal of Physical Oceanogra-*
527 *phy*, 43(2), 259–282. doi: 10.1175/JPO-D-11-0194.1
- 528 Watts, D. R., Tracey, K. L., Donohue, K. A., & Chereskin, T. K. (2016). Estimates
529 of eddy heat flux crossing the antarctic circumpolar current from observations
530 in drake passage. *Journal of Physical Oceanography*, 46(7), 2103-2122. doi:
531 10.1175/JPO-D-16-0029.1
- 532 Youngs, M. K., Thompson, A. F., Lazar, A., & Richards, K. J. (2017). ACC Me-
533 anders, Energy Transfer, and Mixed Barotropic–Baroclinic Instability. *Journal of*
534 *Physical Oceanography*, 47(6), 1291–1305. doi: 10.1175/JPO-D-16-0160.1
- 535 Zika, J. D., Le Sommer, J., Dufour, C. O., Molines, J.-M., Barnier, B., Brasseur, P.,
536 ... Vivier, F. (2013). Vertical Eddy Fluxes in the Southern Ocean. *Journal of*
537 *Physical Oceanography*, 43(5), 941–955. doi: 10.1175/JPO-D-12-0178.1